JAAS

Dynamic Article Links

Cite this: *J. Anal. At. Spectrom.*, 2012, **27**, 232

www.rsc.org/jaas

PAPER

Theoretical calculations of the influence of resonant Raman scattering on the quantification of XRF spectrochemical analysis

Héctor Jorge Sánchez,* María Cecilia Valentinuzzi and Juan José Leani

Received 27th July 2011, Accepted 9th November 2011
DOI: 10.1039/c1ja10219b

In this work we present theoretical calculations of the resonant Raman scattering contributions to the background of X-ray fluorescence spectra. The main goal of the paper is to obtain a simple and reliable procedure to calculate the influence of RRS in spectrochemical analysis by X-ray fluorescence including second order enhancement processes. In order to perform the calculations, the Shiraiwa and Fujino model was used to calculate the characteristic intensities of the different atomic processes involved. In the case of polychromatic excitation over a multi-element sample of proximate atomic numbers, the calculations show that the contribution of RRS is higher than Compton scattering but lower than coherent scattering, this last process being the most important source of background in the range of the fluorescent lines. The calculated effects of enhancements are rather low and have influence only on the lightest elements of the spectra. On the other hand, the resonant Raman scattering line interferes with fluorescent peaks in the case of monochromatic excitation when elements of proximate atomic numbers are analyzed (for example Al–Si). The model proposed here allows the analysis of the different sources of background, which contribute to a better understanding of the physical processes involved in the different techniques of XRF analysis. In addition, the calculations presented here can contribute significantly to a more precise quantification of traces and minor components.

Introduction

X-Ray fluorescence (XRF) analysis is a well established technique for elemental analysis in a variety of samples. Because it does not require complex or time-consuming sample preparation and it is not destructive, XRF is especially suitable for analysis of solid samples.[1–3] It is widely used for spectrochemical analysis in various industries, environmental monitoring, geology, biology, medical applications, *etc.*[4–6]

With ordinary XRF setups, in normal conditions, spectrochemical analysis at the trace level is difficult to achieve, in part due to the systematic errors caused by matrix effects. In XRF the background is caused by interactions of radiation with matter, mainly by elastic and inelastic scattering of the primary photons on the sample and substrate.[7] Background, especially in the low energy region, is mainly due to Compton backscattering of high bremsstrahlung photons from the detector crystal.

By using synchrotron radiation, the TXRF technique has been successfully applied to detect very low concentrations of impurities on Si wafer surfaces with optimum sensitivities.[8,9] The study of light elements ($Z < 14$) is a new challenge: the K-fluorescent signals are about a factor of 30 smaller than the ones of the medium Z elements due to a reduced fluorescence yield, and the Si fluorescent signal tends to dominate the spectrum. These limitations can be overcome with synchrotron radiation since it offers several advantages over conventional X-ray tubes, *e.g.* a high incident flux, low divergence, linear polarization, *etc.*[10,11] These characteristics lead to an increased fluorescent signal while reducing the elastically scattered background. In addition, higher fluorescent intensities can be achieved tuning the energy of the incident photons to a characteristic absorption edge of an element present in the sample, maximizing the cross-section for this element.

An interesting example is the determination of Al impurities on Si wafers. In order to suppress the strong substrate signal, which dominates the spectrum, the energy of the primary radiation is tuned below the Si K absorption edge. This case represents a challenge, since the Al K-absorption edge is just 260 eV below the Si K-edge; however, monochromatic photons provided by a synchrotron source can be employed to solve the problem. Unfortunately, there is a significant increase of the background, starting at about 100 eV below the excitation energy and extending to lower energies by several hundreds of eV.[12]

Resonant Raman scattering (RRS) is an inelastic scattering process that becomes important when the incident radiation energy approaches from below to an absorption edge.[13] This scattering process worsens detection limits by increasing the background of the XRF spectra; in particular, it affects the correct detection and subsequent quantification mainly of minor and trace elements. In order to determine an accurate achievable sensitivity, the shape of the background must be considered. The

Facultad de Matemática, Astronomía y Física, Universidad Nacional de Córdoba, 5000 Córdoba, Argentina. E-mail: jsan@famaf.unc.edu.ar

Raman peak shape is non-symmetric, showing a Gaussian-like shape to the high energy side of the peak and a long smooth tail to the low energy side of the peak. As the incident energy increases the RRS contribution becomes more important and, at the resonant conditions, it is dominant.

The Raman effect was first observed by Sparks in 1974 (ref. 14) and explained theoretically by Bannet and Freund one year later.[15] The theoretical description of the RRS process proceeds from the Kramers–Heisenber equation in time dependent perturbation theory:[13]

$$H_{\text{int}} = \sum_j \frac{e^2}{2mc^2} \boldsymbol{A}_j^2 - \sum_j \frac{e}{mc} \boldsymbol{p}_j \boldsymbol{A}_j \tag{1}$$

where $\boldsymbol{p_j}$ is the momentum of the j^{th} target electron and $\boldsymbol{A_j}$ the vector potential of the electromagnetic field. e and m are the charge and mass of the electron and c the speed of light. The $\boldsymbol{A^2}$ term is responsible for scattering (including diffraction and non-resonant inelastic scattering), whereas $\boldsymbol{p} \times \boldsymbol{A}$ is related to the absorption processes and resonant scattering. Depending on the energy and the momentum transfer in the inelastic scattering process, quite distinct information can be obtained. The RRS effect appears from the $\boldsymbol{p} \times \boldsymbol{A}$ term in the Hamiltonian's interaction between the incident photon and the atomic electron.

According to the Kramers–Heisenberg equations, the theoretical expression of the differential RRS cross-section for one electron and one resonant term is:

$$\frac{\mathrm{d}\sigma(E_0, E_S)}{\mathrm{d}E_S} = \left(\frac{E_S}{E_0}\right) \left(\frac{e^2}{mc^2}\right)^2 c \int \frac{(1 - n_{\vec{k}})\ |M_{fi}|^2 \delta(E_0 - E_s - (u_{\vec{k}} + \Omega_L)) d^3k}{8\pi^3} \tag{2}$$

being

$$M_{fi} = \frac{\langle P|\vec{p}\vec{u}_2|S\rangle \langle k|\vec{p}\vec{u}_1|S\rangle}{m(E_0 - u_k - \Omega_k + i\Gamma_K)} \tag{3}$$

where the states $|S\rangle$ and $|P\rangle$ are the one-electron wave functions for the bound K- and L-shell electrons, Γ_K is the lifetime of the K shell, the $|k\rangle$ state represents the conduction electron wave functions with a Fermi function u_k, $\vec{u}_1$ and $\vec{u}_2$ correspond to the polarization state. When the incident energy is below the absorption edge, eqn (2) becomes:

$$\frac{\mathrm{d}\sigma(E_0, E_S)}{\mathrm{d}E_S} = G(E_0, E_S)\ \frac{E_S}{(\Omega_K - \Omega_L - E_S)^2 + \Gamma_K^2} \tag{4}$$

where $G(E_0,E_S)$ is an absorption factor, evaluated at $E_0 = \Omega_L - \Omega_K + E_S$.

Different types of the RRS process have been experimentally distinguished, depending on which shell the vacancy is created, *i.e.* KL-RRS denotes a vacancy created in the K shell and an L-shell hole created in the final state. In this way, transitions type KM-RRS, KN-RRS, and LM-RRS can be considered.

Fig. 1 represents the scattering process when the incident photon has energy below the K-absorption edge and the K hole is filled by an electron from the L shell (KL-type scattering). The incident photon has energy E_0 lower than the Ω_K energy of the K edge; the energy of the incident photon is absorbed by a K-shell electron producing a hole and an electron in the continuum with kinetic energy k_e. The K shell vacancy is filled by an electron from the L shell (being Ω_L the energy of the L threshold) and a scattered photon is emitted with energy E_S. Assuming a well defined energy of the incident photon, the energy conservation for the scattering process leads to:

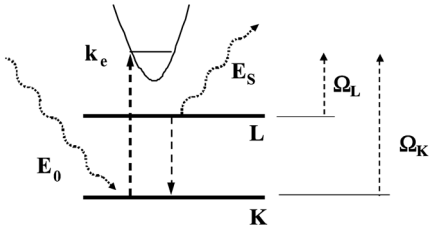

Fig. 1 Schematic representation of a KL resonant Raman scattering process. The incident photon has energy E_0 lower than the Ω_K energy of the K edge; this photon is absorbed by a K-shell electron producing a hole and an electron in the continuum with kinetic energy k_e. The K shell vacancy is filled by an electron from the L shell (being Ω_L the energy of the L threshold) and a scattered photon is emitted with energy E_S.

$$E_0 - \Omega_L - e_f = E_S + k_e \tag{5}$$

where e_f is the Fermi energy. This equation indicates that between initial and final states the available energy has to be shared between the outgoing electron and the emitted photon.

In specific experimental conditions the resonant Raman effect must be taken into account when samples, constituted by elements with proximate atomic numbers, are analyzed because this process affects the determination of low concentration contaminants. In addition, the experimental values of mass attenuation coefficients differ from the theoretical values when materials are analyzed with monochromatic X-ray beams under resonant conditions. The resonant Raman scattering is in part responsible for this discrepancy.

In order to study the Raman effect, radiation emitted by X-ray tubes and synchrotron sources has been employed.[16,17] The use of proton induced monochromatic X-ray beams has also been reported; these systems were used to make measurements of KL and KM-RRS cross-sections of several elements from Al to Hf.[12,13,18,19]

KL-RRS cross-sections have been determined for elements such as Cr, Mn, Fe, Ni, Cu, Zn, and Zr. Besides, KL-RRS cross-sections were determined as a function of the incident energy employing theoretical models for the energy distribution of the Raman scattered photons, convoluted with the instrument function.[20]

In this work we present theoretical calculations of the resonant Raman scattering contributions to background of X-ray fluorescence spectra. The calculations show that in the case of X-ray tube excitation the RRS prevails over Compton scattering except in the low energy region, and Raman enhancements are very weak, affecting only the lightest elements. Nevertheless, the Raman contribution becomes important when a monochromatic source is employed and elements of proximate atomic numbers are analyzed.

Calculations

The basic procedure to calculate fluorescent intensities was presented by Sherman in 1955 (ref. 21) and Shiraiwa and

Fujino in 1966.[22] Corrections to these equations were proposed later by Li-Xing in 1984 (ref. 23) and Fernández and Rubio in 1989.[24]

In those works, several assumptions, approximations and considerations were made, regarding the geometry of the X-ray beam and sample, physical constants and parameters, *etc.* The same assumptions are applied in this work.

Unlike fluorescent processes and coherent or Compton scattering, the Raman scattering presents a scattered energy distribution for a given incident energy; therefore the emission factor for Raman interactions can be expressed as:

$$Q_i^r(E,E') = \int_0^{E-\Omega_{Li}+e_f} \frac{H^R(E)\ C_{\ i}\ E'}{(\Omega_{Ki}-E)\left[\ (\Omega_{Ki}-\Omega_{Li}-E')^2-e_f^2\right]}\,dE' \quad (6)$$

This expression derives from eqn (4). The factor $H^R(E)$ was defined in ref. 20. It takes into account the absorption and emission efficiency of the scattered photons and depends on the element and on the energy of the incident photons.

The emission factors for fluorescence, coherent and Compton scattering are

$$Q_{ip}^f(E) = C_i\omega_{ip}J_{ip}f_{ip}\tau_i(E),$$

$$Q^c(E) = \sum_j C_j\sigma_j^c(E)$$

and

$$Q^i(E) = \sum_j C_j\sigma_j^i(E)$$

respectively. The notation regarding the emission factors, the equations, and Fig. 2 and 3 is shown in Table 1.

In the present calculations K_α and K_β lines will be considered, enhancements effects (second order interactions) will be calculated and the intrinsic resolution of the detection system will be taken into account. In this way, the obtained results will reflect the main characteristics of XRF spectra. On the other hand, infrared divergence of the Compton scattering[25] and bremsstrahlung processes will be neglected since they contribute to the low energy range of the spectrum, which is in general out of the region of the elements of interest.

The same approach used in the papers of ref. 21–24 will be used in this work. Thus, the attenuations and interaction processes of the photons inside the sample (for both the incident and the emerging beams) are considered (Fig. 2). The primary intensities for element i are obtained through the following equation:

$${}^1I_j^x(E) = \int_0^{E_{max}} \frac{\Delta}{4\pi}\frac{I_0(\tilde{E})Q_i^x(\tilde{E},E)}{\mu_s(\tilde{E})-\mu_s(E)G}d\tilde{E} \quad (7)$$

where x stands for fluorescent (f), coherent (c), incoherent (i) or Raman (r) interactions respectively; in the case of fluorescent interactions, K_α and K_β lines must be considered separately.

In order to obtain an expression that reproduces similar spectra to those obtained with a spectrometer with a real detection system, eqn (3) must be convoluted with the detector function:

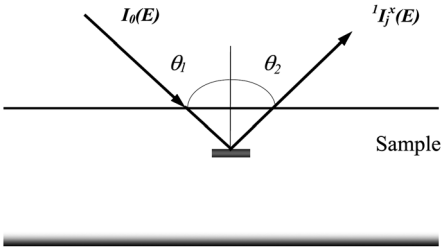

Fig. 2 Schematic of incident and emerging beams for first-order interactions. I_0 is the intensity of the incident beam and ${}^1I_j^x$ is the intensity emitted by element i after an x-type process (1 stands for primary interaction). θ_1 and θ_2 are the incident and takeoff angles, respectively, measured from the normal to the sample surface.

$$\Gamma(E,E') = \frac{e^{-(E-E')^2/2\delta^2}}{\sqrt{2\pi}\delta} \quad (8)$$

Consequently, the primary intensity for element i is then expressed as:

$${}^1I_j^x(E) = \int_0^{E_{max}}\int_0^{E_{max}} \frac{\Delta}{4\pi}\frac{I_0(\tilde{E})Q_i^x(\tilde{E},E')}{\mu_s(\tilde{E})-\mu_s(E')G}d\tilde{E}\,\frac{e^{-(E-E')^2/2\delta^2}}{\sqrt{2\pi}\delta}\,dE' \quad (9)$$

being E' the energy of the photons emitted by element i as a result of the process x.

Second order effects are studied considering the geometrical arrangement given in Fig. 3. From the analysis of beam trajectories, interactions and attenuations, and after partial volumetric integrations, a general expression for the enhancement intensity of each interaction is obtained:

$$\begin{aligned}{}^2I_i^{x,y}(E) = \sum_{k=1}^{N}\int_0^{E_{max}} \frac{\Delta}{8\pi}\frac{I_0(\tilde{E})Q_k^x(\tilde{E},E'')Q_i^y(E'',E')}{\mu_s(\tilde{E})-\mu_s(E')G} \\ \left\{\frac{\cos\theta_1}{\mu_s(\tilde{E})}\ln\left[1+\frac{\mu_s(\tilde{E})}{\mu_s(E'')\cos\theta_1}\right]\right. \\ \left.+\frac{\cos\theta_2}{\mu_s(E')}\ln\left[1+\frac{\mu_s(E')}{\mu_s(E'')\cos\theta_2}\right]\right\}d\tilde{E}\end{aligned} \quad (10)$$

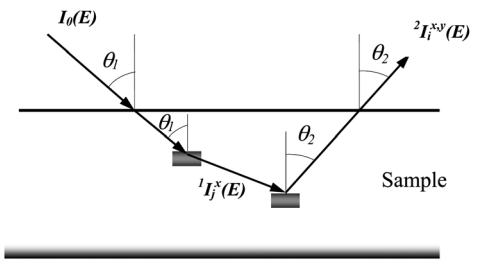

Fig. 3 Schematic of incident, internal and emerging beams for second-order interactions. I_0 is the intensity of the incident beam, ${}^1I_j^x$ is the intensity of internal beam emitted by element i after an x-type process (^{1} stands for primary interaction) and ${}^2I_i^{x,y}$ is the intensity emitted by element i after a y-type process induced by an x-type process (^{2} stands for second-order interaction). θ_1 and θ_2 are the incident and takeoff angles, respectively, measured from the normal to the sample surface.

Table 1 Notation of the equations described in the text

Symbol	Definition
$H^{R}(E)$	Normalization factor for Raman scattering[23]
R_Z	Concentration of element i multiplied by its fluorescent yield
Ω_{Ki}, Ω_{Li}	Binding energies for the i line of the K and L edge respectively
e_f	Fermi energy
E	Energy of the incident beam
Δ	Solid angle subtended by the detector
I_0	Intensity of the incident beam
E_{max}	Maximum energy of the incident X-ray beam
$\tau_i(E)$	Mass photoabsorption coefficient of element i at energy E
$\sigma_j^c(E)$, $\sigma_j^i(E)$	Total coherent (c) and incoherent (i) scattering cross-sections for element j at energy E
$\mu_i(E)$	Mass attenuation coefficients of element i at energy E
$\mu_s(E)$	Mass attenuation coefficients of the sample defined as: $\mu_s(E) = \sum_i C_i\mu_i(E)$
$Q_{ip}^f(E)$	Fluorescent emission factor of the sample for line p of element i
$Q^c(E)$, $Q^i(E)$	Coherent (c) and incoherent (i) scattering emission factor of the sample
ω_{ip}	Fluorescence yield of element i, line p
J_{ip}	Absorption edge jump for line p of element i
f_{ip}	Emission probability of line p, element i
C_i	Concentration of element i in the sample
G	Geometrical factor given by $G = \cos\theta_1/\cos\theta_2$
θ_1,θ_2	Incident and takeoff angles measured from the normal to the sample surface
δ	Intrinsic resolution of the detection system
${}^1I_j^x$	Intensity emitted by element i after an x-type process; "1" stands for primary interaction
${}^2I_i^{x,y}$	Intensity emitted by element i after a y-type process induced by an x-type process; "2" stands for second-order interaction

where x,y stand for fluorescent (f), coherent (c), incoherent (i) or Raman (r) interactions respectively. This expression represents the intensity of photons emitted after a y process excited by the photons emitted after an x process inside the sample. E' is the energy of the photons emitted by element i as a result of the x process and E'' is the energy of the photons emitted by the y process. Again, K_α and K_β fluorescent emissions are considered.

Finally, after convolution with the resolution function, the following expression is obtained:

$$
{}^2I_i^{x,y}(E) = \int_0^{E_{max}} \sum_{k=1}^{N} \int_0^{E_{max}} \frac{\Delta}{8\pi} \frac{I_0(\tilde{E})Q_k^x(\tilde{E},E'')Q_i^y(E'',E')}{\mu_s(\tilde{E}) - \mu_s(E')G} \left\{ \frac{\cos\theta_1}{\mu_s(\tilde{E})} \ln \left[1 + \frac{\mu_s(\tilde{E})}{\mu_s(E'')\cos\theta_1} \right] + \frac{\cos\theta_2}{\mu_s(E')} \ln \left[1 + \frac{\mu_s(E')}{\mu_s(E'')\cos\theta_2} \right] \right\} d\tilde{E} \frac{e^{-(E-E')^2/2\delta^2}}{\sqrt{2\pi}\delta} d\hat{E} \quad (11)
$$

being E' and E'' defined in eqn (10).

It must be taken into account that due to all the possible interactions, there are sixteen second order processes, according to all x,y combinations among fluorescent, coherent and incoherent scattering and Raman interactions, including self-interactions.

Calculations were performed using MathCAD 13.[26] Integrations were accomplished by a Newton procedure for numerical integration and not using the internal routine of MathCAD in order to avoid divergences during calculations. Mass attenuation coefficients were taken from Hubbell and Seltzer,[27] emission probabilities were obtained from Scofield[28,29] and Khan and Karimi,[30] fluorescence yields were taken from the compilation of Hubbell *et al.*,[31] and the energies of the emission and absorption lines were those compiled by Bearden,[32] Birks,[33] and Bearden and Burr.[34] For the convolutions with the detector function, a typical Si(Li) solid-state detector was considered with a resolution of 145 eV for the Mn Kα line.

As a first stage, a sample irradiated by a continuum spectrum emitted from a Mo X-ray tube at 45 kV was considered. It was represented mathematically according to the procedure described in ref. 35 using typical parameters of X-ray tubes used in spectroscopy. The analyzed sample consisted of a multi-elemental target with 15% Mn, 1% Fe, 6% Ni, 53% Cu and 25% Zn, which represents the composition of a typical standard bronze.

The next stage consisted of calculations performed with monochromatic incident radiation. The sample under consideration was Al impurities on Si due to the important role of this material on TXRF as a reflector substrate.[36,11] The contribution of the Raman scattering must be identified for a proper analysis. The considered specimen consisted of a Si (99.95%) sample contaminated with 0.05% of Al. The energy of excitation for calculations was 1739 eV, which is above the Al absorption edge and below the Si absorption edge.

Finally, we carried out calculations for two additional binary samples. These samples were studied because of the relevance of their applications and the importance of the enhancements effects. On one hand, a binary alloy of Fe with traces of Mn was studied because of its importance in the stainless steels industries. On the other hand a pure sample of Ti with V traces was analyzed due to the current relevance in medical applications. The concentrations under analysis were Mn (0.01%) and Fe (99.99%) and a sample of Ti (99%) contaminated with V (1%). The incident spectrum of a Mo X-ray tube at 45 keV was considered because this source of photons is the most common device used during the analysis of these kinds of alloys.

Results and discussion

Fig. 4 shows the result of the calculations for the bronze sample irradiated by a Mo X-ray tube. The fluorescent line intensities, and the total contributions (first and second order) of incoherent, coherent, and Raman scattering are showed. According to these results, coherent scattering prevails over the other types of scattering, the resonant Raman scattering presents a more important contribution than the Compton background in almost all the spectrum (except in the very high energy region), and especially under the elements-of-interest area.

Fig. 5 shows the calculated background due to all scattering interactions and only due to Raman scattering. This figure indicates that Raman scattering contributes to the background only in the low energy zone, far away from the range of the

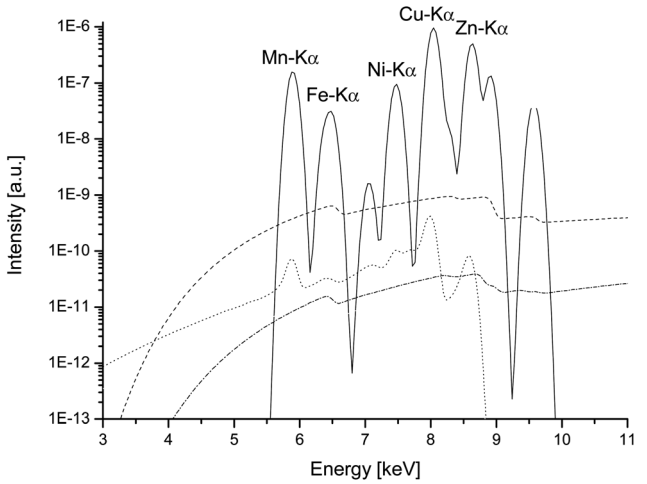

Fig. 4 Results of calculations for fluorescent lines (solid line), coherent (dashed line), incoherent (dashed-dotted line) and Raman scattering (dotted line). It was considered a multi-elemental target (typical bronze) irradiated by a continuum spectrum emitted from a Mo X-ray tube at 45 kV.

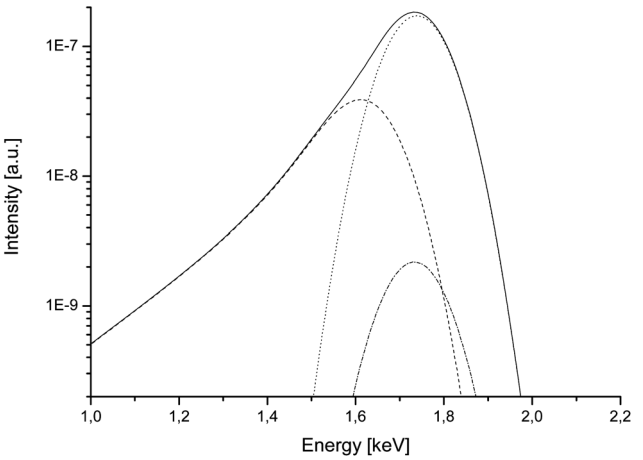

Fig. 6 Total background (solid line) calculated considering the contributions from Raman scattering (dotted line), coherent scattering (dashed line) and incoherent scattering (dashed-dotted line). The sample consisted of a Si (99.95%) substrate contaminated with 0.05% of Al. The monochromatic energy of excitation was 1739 eV.

elements-of-interest that compose the sample; nevertheless at lower energy levels other artifacts like infrared divergence of the Compton scattering or bremsstrahlung processes would compete with these typical sources of background.

Fig. 6 shows the result of the calculations for the Al–Si sample irradiated with monochromatic radiation. As can be seen, the most important contribution is from the coherent scattering process; however, the Raman contribution turns out to be considerable since it is located at the left of the scattering peak (corresponding to lower energies), resulting in a final contribution with an asymmetric shape. Then the Al fluorescent peak is affected, as it is shown in Fig. 7.

The low-energy side of the shape of the Raman peak affects the Al fluorescent peak and its contribution must be considered during quantification. In order to evaluate the influence of the Raman contribution, a quantitative calculus procedure, using the AXIL package[37] and based on fundamental parameters, was performed. The considered specimen was specified above and the calculated intensities were used for quantification (as theoretical calculations of intensities are employed, the experimental constant is not present and no standards are required). The concentration obtained by the fundamental parameter method[38] for Al if the Raman scattering is not taken into consideration is 0.32%, that is six times higher than its real value (0.05%). This comparison cannot be performed under experimental conditions because it is impossible to discriminate the Raman scattering from the total background. These results point out the importance of taking into account all the atomic interactions for a proper quantification with the fundamental parameter method.

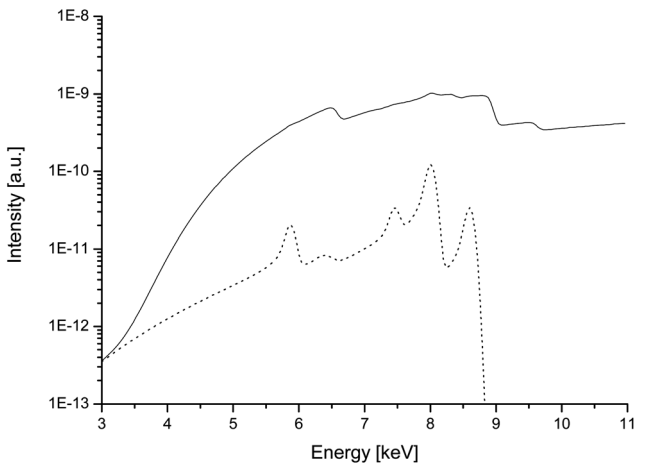

Fig. 5 Calculated total background (black line) and due only to Raman scattering (dotted line). It was considered a multi-elemental target (typical bronze) irradiated by a continuum spectrum emitted from a Mo X-ray tube at 45 kV.

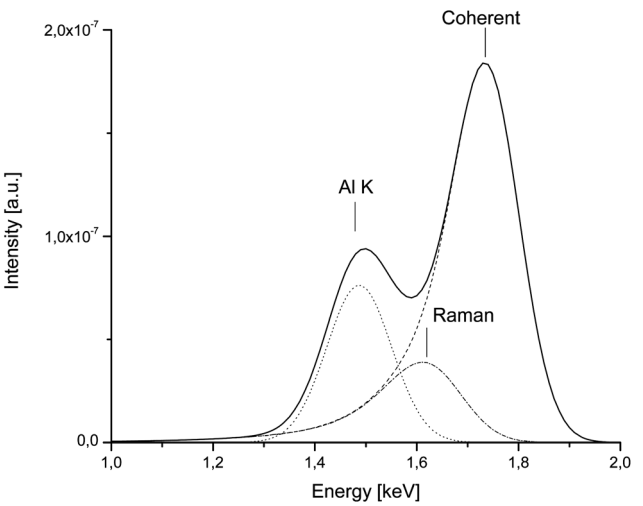

Fig. 7 Calculated measured spectrum (solid line) calculated with total fluorescence (dotted line) and total background (dashed line). Raman scattering contribution is also shown (dashed-dotted line). The sample consisted of a Si (99.95%) substrate contaminated with 0.05% of Al. The monochromatic energy of excitation was 1739 eV.

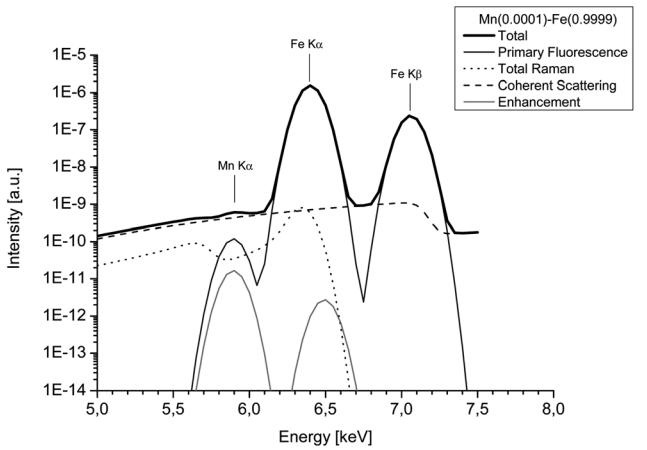

Fig. 8 Results of calculations for primary fluorescence (dark grey), Raman scattering (dotted line), coherent scattering (dashed line), enhancement (secondary fluorescence) (light gray line) and total spectrum (black line) for the binary alloy of Fe with traces of Mn. An incident spectrum of a Mo X-ray tube at 45 keV was considered.

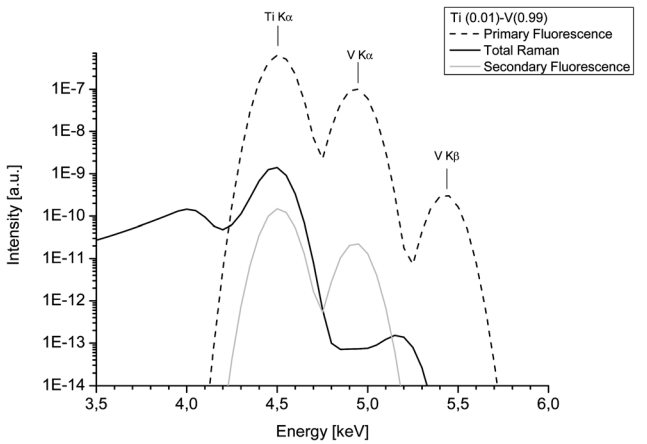

Fig. 9 Results of calculations for primary fluorescence (dashed line), Raman scattering (black line) and secondary fluorescence (light gray line) for a sample of Ti with V traces. An incident spectrum of a Mo X-ray tube at 45 keV was considered.

On the other hand, it should be pointed out that the example considered above is a very special case where Raman scattering is quite significant. Nevertheless, nowadays monochromatic synchrotron radiation is used almost everyday to measure trace elements and Raman effects become more frequent and significant.

Fig. 8 shows the different sources of background (only coherent and Raman) and the fluorescent lines for the Mn–Fe alloy. As can be seen, the Raman contribution under the Mn peak (5.9 keV) is higher than the coherent background and one order of magnitude higher than the secondary fluorescent emissions. In addition, in the low energy region, the contribution of the Raman scattering from Fe turns out to be critical since it is located under the Mn fluorescent peak, resulting in a final contribution with an asymmetric shape and a spurious peak at 5.65 keV.

The contribution of Raman scattering to the background of the Ti–V alloy is shown in Fig. 9. As can be observed, the Raman contribution from V affects the Ti fluorescent peak and its contribution must be considered during quantification in order to obtain accurate and reliable results.

It is interesting to note that in all cases showed above, the contribution of the Raman scattering to the background is higher than the enhancement effects (secondary fluorescence), which means that realistic algorithms for quantification should take into account Raman scattering at least as much as enhancements.

These results show that in specific experimental conditions the resonant Raman scattering must be taken into account when samples, constituted by elements with proximate atomic numbers, are analyzed because this process affects the determination of low concentration contaminants. In addition, the experimental values of mass attenuation coefficients differ from the theoretical values when materials are analyzed with monochromatic X-ray beams under resonant conditions. These results indicate that resonant Raman scattering is responsible for this discrepancy.

Conclusions

A simple and reliable procedure was presented to calculate the resonant Raman scattering contributions to the X-ray fluorescence spectra. It was applied to both polychromatic and monochromatic radiation exciting typical samples in spectrochemical studies. The used algorithm includes second order interactions which can be evaluated and quantified for each sample under consideration. To the authors knowledge this was not reported previously.

According to the obtained results, the Raman scattering does not significantly contribute to the XRF spectra when excitation is performed with polychromatic radiation, as is the case of X-ray tubes. Neither the enhancement effects suffered by fluorescent radiation nor the influence of the scattering background have a significant influence on the quantification in the spectrochemical analysis of the sample. Only appreciable effects would be observed in the lightest elements present in the specimen or when the sample is composed of elements with proximate atomic numbers.

On the other hand, the resonant Raman scattering contributes to the background in X-ray spectrochemical analysis when monochromatic radiation is used to excite elements with proximate atomic numbers. The presence of Raman background reduces detection limits and interferes with fluorescent peaks.

More resonant Raman scattering cross-sections have to be investigated and quantified in order to be included in the calculations of total attenuation of X-rays in matter. It is very important to understand the behavior of this scattering process and to quantify its occurrence probability.

With the assistance of the present algorithm, further calculations (in diverse excitation conditions) with monochromatic incident radiation and different constitutive elements will reveal the Raman scattering contribution to the XRF spectra in a variety of experimental situations.

The algorithm presented in this work could be improved with the incorporation of other secondary interactions affecting the low energy range, like infrared divergence and bremsstrahlung processes. The future addition of these effects to the algorithm

will account for the analysis of low-Z elements in the low energy range.

References

1 B. M. Gordon, A. L. Hanson, K. W. Jones, J. G. Pounds, M. L. Rivers, G. Schidlovsky, P. Spanne and S. R. Sutton, *Nucl. Instrum. Methods Phys. Res., Sect. B*, 1990, **45**, 527.
2 K. Janssens, L. Vincze, B. Vekemans, A. Aerts, F. Adams, K. W. Jones and A. Knochel, *Mikrochim. Acta*, 1996, **13**, 87.
3 K. Jansses, L. Vincze, F. Adams and K. W. Jones, *Anal. Chim. Acta*, 1993, **283**, 98.
4 H. J. Sánchez and M. C. Valentinuzzi, *X-Ray Spectrom.*, 2006, **35**, 379.
5 M. C. Valentinuzzi, H. J. Sánchez and J. Abraham, *Spectrochim. Acta, Part B*, 2006, **61**, 1175.
6 E. D. Greaves, L. M. Marcó Parra, A. Rojas and L. Sajo-Bohus, *X-Ray Spectrom.*, 2000, **29**, 349.
7 H. Aiginger and P. Wobrauschek, *Adv. X-Ray Anal.*, 1984, **28**, 1.
8 P. Pianetta, N. Takaura, W. Brennan, S. Tompkins, S. Laderman, A. Fischer Colbrie, A. Shimazaki, K. Miyazaki, M. Madden, D. C. Wherry and J. B. Kortright, *Rev. Sci. Instrum.*, 1995, **66**, 1293.
9 F. Comin, M. Navizet, P. Mangiagalli and G. Apostolo, *Nucl. Instrum. Methods Phys. Res., Sect. B*, 1999, **150**, 538.
10 M. Müller, B. Beckhoff, G. Ulm and B. Kanngieβer, *Phys. Rev. A: At., Mol., Opt. Phys.*, 2006, **74**(1), 012702.
11 K. Baur, J. Kerner, S. Brennan, A. Singh and P. Pianetta, *J. Appl. Phys.*, 2000, **88**, 4642–4647.
12 P. Singh, D. Mehta, N. Singh, S. Puri and J. S. Shahi, *Nucl. Instrum. Methods Phys. Res., Sect. B*, 2004, **225**, 198–206.
13 A. G. Karydas and T. Paradellis, *J. Phys. B: At., Mol. Opt. Phys.*, 1997, **30**, 1893–1905.
14 C. J. Sparks, Jr, *Phys. Rev. Lett.*, 1974, **33**, 262–265.
15 Y. B. Bannet and I. Freund, *Phys. Rev. Lett.*, 1975, **34**, 372–376.
16 P. Suortti, *Phys. Status Solidi B*, 1979, **91**, 657–666.
17 Ch. Zarkadas, A. G. Karydas, M. Müller and B. Beckhoff, *Spectrochim. Acta, Part B*, 2006, **61**, 189–195.
18 A. G. Karydas, M. Budnar, Z. Smit, Ch. Zarcadas and T. Paradellis, *Nucl. Instrum. Methods Phys. Res., Sect. B*, 2002, **189**, 43–48.
19 P. Singh, D. Mehta, N. Singh, S. Puri and J. S. Shahi, *Nucl. Instrum. Methods Phys. Res., Sect. B*, 2004, **225**, 198–206.
20 H. J. Sánchez, M. C. Valentinuzzi and C. Pérez, *J. Phys. B: At., Mol. Opt. Phys.*, 2006, **39**, 1–11.
21 J. Sherman, *Spectrochim. Acta*, 1955, **7**, 283.
22 T. Shiraiwa and N. Fujino, *Jpn. J. Appl. Phys.*, 1966, **5**, 886.
23 Z. Li-Xing, *X-Ray Spectrom.*, 1984, **13**, 52.
24 J. Fernández and M. Rubio, *X-Ray Spectrom.*, 1989, **18**, 281.
25 Y. B. Bannet, D. C. Rapaport and I. Freund, *Phys. Rev. A: At., Mol., Opt. Phys.*, 1977, **16**, 2011.
26 Mathsoft Engineering & Education, Inc., www.ptc.com/products/mathcad/.
27 J. M. Hubbell and S. M. Seltzer, *Tables of X-Ray Mass Absorption Coefficients and Mass Energy*, NISTIR 5632, 1995.
28 J. H. Scofield, *Phys. Rev.*, 1969, **179**, 9.
29 J. H. Scofield, *Phys. Rev. A: At., Mol., Opt. Phys.*, 1974, **9**, 1041.
30 Md. R. Khan and M. Karimi, *X-Ray Spectrom.*, 1980, **9**, 32.
31 H. Hubbell, P. N. Trehan, N. Singh, B. Chand, D. Mehta, M. L. Garg, R. R. Garg, S. Singh and S. Puri, *J. Phys. Chem. Ref. Data*, 1994, **23**, 339.
32 J. A. Bearden, *Rev. Mod. Phys.*, 1969, **39**, 78.
33 L. S. Birks, in *Handbook of Spectroscopy*, CRC Press, Cleveland, OH, 1974, p. 3.
34 J. A. Bearden and A. F. Burr, *Rev. Mod. Phys.*, 1967, **39**, 125.
35 R. Mainardi and R. Barrea, *X-Ray Spectrom.*, 1996, **25**, 190.
36 J. Szlachetko, C. L. Dousse, J. Hoszowska, M. Pajek, R. Barret, M. Berset, K. Fennane, A. Kubala-Kukus and M. Szlacheto, *Phys. Rev. Lett.*, 2006, 1–4, PRL 97 073001.
37 P. Van Espen, H. Nullens and F. Adams, *Nucl. Instrum. Methods*, 1977, **142**, 243–250.
38 W. Brefeld and P. Gurtler, *Handbook of Synchrotron Radiation*, Elsevier Science, 1991, vol. 4.